Lithium superionic conductors with corner-sharing frameworks

KyuJung Jun[1,2,5], Yingzhi Sun[1,2,5], Yihan Xiao[1,2], Yan Zeng[2], Ryounghee Kim[4], Haegyeom Kim[2], Lincoln J. Miara[3], Dongmin Im[4], Yan Wang[3,*], and Gerbrand Ceder[1,2,*]

1. Department of Materials Science and Engineering, University of California Berkeley, Berkeley, CA 94720, USA

2. Materials Sciences Division, Lawrence Berkeley National Laboratory, Berkeley, CA 94720, USA

3. Advanced Materials Lab, Samsung Advanced Institute of Technology-America, Samsung Semiconductor Inc., Cambridge, MA 02138, USA

4. Next Generation Battery Lab, Samsung Advanced Institute of Technology, Samsung Electronics Co., Ltd., Suwon, Korea

5. These authors contributed equally.

* Correspondence: eric.wangyan@samsung.com, gceder@berkeley.edu

Abstract

Superionic lithium conductivity has only been discovered in a few classes of materials, mostly found in thiophosphates and rarely in oxides. Herein, we reveal that corner-sharing connectivity of the oxide crystal structure framework promotes superionic conductivity which we rationalize from their distorted lithium environment and reduced interaction between lithium and non-Li cations. By performing a high-throughput search for materials with this feature, we discover 10 novel oxide frameworks predicted to exhibit superionic conductivity—from which we experimentally demonstrate $LiGa(SeO_3)_2$ with a bulk ionic conductivity of 0.11 mS/cm and activation energy of 0.17 eV. Our findings provide new insight into the factors that govern fast lithium mobility in oxide materials and will accelerate the development of novel oxide electrolytes for all solid-state batteries.

All-solid-state batteries are increasingly attracting attention as next-generation energy storage devices for application in consumer electronics and electric vehicles[1]. The all-solid-state design replaces the flammable organic liquid electrolyte in conventional batteries with an inorganic solid electrolyte and enables the use of high-energy electrodes, resulting in enhanced safety and high energy density[2]. A critical factor for the realization of such batteries is the development of solid electrolytes (SEs) with high ionic conductivity and excellent electrochemical stability against both a lithium-metal anode and high-voltage cathodes[3]. While high ionic conductivity obviously reduces cell impedance and may increase the active materials loading in the cathode composite[4], it has recently also been shown to reduce the build-up of mechanical stress in the lithium metal anode[5].

Several sulfide-based inorganic solid electrolytes, such as $Li_{10}GeP_2S_{10}$ (LGPS)[6], $L_7P_3S_{11}$[7], and Li argyrodites[8] exhibit high lithium ionic conductivity (>10 mS/cm) exceeding that of liquid electrolytes[6,7,9]. However, the limited chemical and electrochemical stability of the sulfides[10-13] and their possible H_2S release upon air or water exposure[14,15] are potential safety concerns for both manufacturing and applications. In contrast, many oxide SEs have shown excellent air and electrochemical stability[11], but their ionic conductivities are generally lower than those of sulfide SEs[16]. Thus far, only a few oxide SEs (*e.g.*, Na superionic conductor (NASICON)-type Li-oxides[17], Li-garnets[18], and Li-perovskites[19]) have been discovered with room-temperature (RT) ionic conductivities (σ_{RT} ¿ on the order of 0.1–1 mS/cm.

Discovery of new fast Li-ion conductors could be accelerated if the structural and chemical features that govern facile lithium movement could be identified. In sulfides, finding superionic conductors has focused on crystal structures that provide a low-barrier ionic pathway between nearly energy-equivalent sites[20] . This has led to the principle that materials with a body-centered-cubic (bcc) arrangement of anions are more desirable than close-packed structures, as this bcc arrangement allows for Li migration through face-sharing tetrahedral sites with low activation energy. This feature has been observed in the

4

best-performing sulfide ionic conductors such as $L_7P_3S_{11}$, LGPS and its derivatives, and was used in the design of a novel class of solid electrolytes $Li_{1+x}Zn_{1-x}PS_4$[21,22].

The guidelines for finding good sulfide Li-ion conductors do not seem as applicable to oxide materials. The hypothetical oxide derivative of LGPS, $Li_{10}GeP_2O_{10}$, is predicted to exhibit ionic conductivity that is two orders of magnitude lower than that of LGPS[23] and has never been synthesized. Similar observations of lower ionic conductivity in oxides than sulfides have been made for LISICONs versus thio-LISICON conductors[24]. The lower ionic conductivity of oxides is primarily attributed to the weaker screening ability of the oxygen anion relative to that of the sulfur anion, and this difference in screening power likely gives the arrangement of the non-lithium cations a larger influence on the lithium mobility in oxides than it does in sulfides[4,25]. While it is the near-sightedness of the cation electrostatics in sulfides that leads to the focus on the anion coordination for conductivity optimization, oxides require a different conceptual framework as the oxygen anion cannot effectively screen away the interaction with the other cations. The lack of design principles for superionic conductors has led to a much lower success rate in finding new oxide conductors in computational screening efforts than has been the case for sulfides[26-31] .

In this work, we identify a corner-sharing framework as a structural feature common to many oxide superionic conductors. By using this feature as a descriptor in high-throughput computational screening, we identify 10 novel oxide structural frameworks that are predicted to exhibit superionic conductivity. The concept is experimentally validated in $LiGa(SeO_3)_2$, a new oxide conductor which shows very high bulk ionic conductivity of 0.11 mS/cm. Our findings suggest that corner sharing in the framework provides access to a highly distorted lithium environment and allows for percolating pathways through which lithium can move with a low energy barrier, thereby explaining the origin of the fast lithium diffusion in multiple known and predicted oxide superionic conductors.

5

A structural commonality of lithium superionic conductors

A typical inorganic Li-ion conductor has a crystal structure with anions serving as a backbone hosting fast-moving lithium and immobile non-lithium cations. Figure 1 presents the structures of three exemplary fast lithium-ion conductors with their non-lithium cation sites visualized as colored polyhedrons. $Li_{1+x}Al_xTi_{2-x}(PO_4)_3$ represents a NASICON-type superionic conductor with experimental σ_{RT} of approximately 3 mS/cm at x=0.3[17,32]. $LiTa_2PO_8$ is a superionic conductor with ionic conductivity of 1.6 mS/cm at RT[33]. $Li_{1+x}Ta_{1-x}Zr_xSiO_5$ has been predicted to be a fast ionic conductor and was successfully synthesized recently[34,35]. With sufficient excess lithium, its ionic conductivity is predicted to reach 6.1 mS/cm at RT.

We argue here that these fast oxide conductors, in addition to 10 other groups of oxide conductors that were previously predicted to be fast conductors (see Supplementary Table 1), have important structural commonality and that this insight can be leveraged to find other fast ionic conductors. The non-lithium cation polyhedrons in these structures are interconnected by a corner-shared oxygen, and never share any common edges (O–O bond) or faces (O–O–O triangle), as shown in Fig. 1d-e. For example, the framework of $Li_{1+x}Al_xTi_{2-x}(PO_4)_3$ consists of corner-shared Ti-octahedrons and P-tetrahedrons. To extract this structural feature in a rigorous manner, we first define the "framework" of a compound as the set of coordination polyhedrons of immobile cations *excluding* lithium. A corner-sharing (CS) framework is defined as a framework in which its polyhedrons are interconnected solely by one anion vertex or less (Fig. 1f–g). Using this definition of a CS framework, we also include frameworks in which polyhedrons are isolated from one another (e.g., the framework of LGPS or LISICON $Li_{2+2x}Zn_{1-x}SiO_4$ with $x > 0$[36,37] (Supplementary Figure 1)). A non-corner-sharing (non-CS) framework is then defined as a framework in which at least one edge or face is shared among the framework polyhedrons (Fig. 1d–e).

6
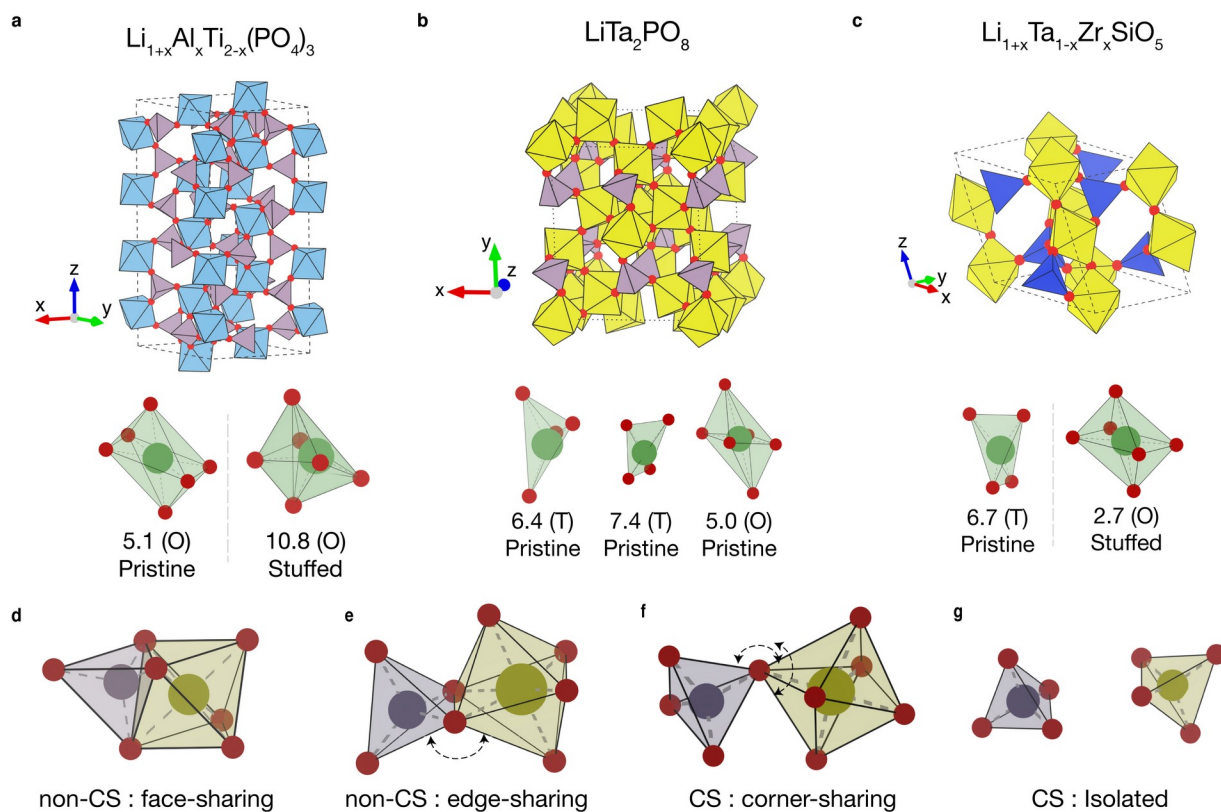
Figure 1. **Crystal structures of known superionic conductors with corner-sharing (CS) frameworks**. *Structures of known CS superionic conductors are shown (a)–(c). The red spheres represent the oxygen atoms at the corner-sharing vertex. The lithium environments in each superionic conductor are shown below each framework. CSM values corresponding to tetrahedral (T) and octahedral (O) geometry of the lithium environment are provided for both the lithium when the composition x is 0 (Pristine) and for the stuffed lithium compound when the composition x is larger than 0 (Stuffed). Light blue, light violet, yellow, and blue polyhedrons represent Ti, P, Ta, and Si sites, respectively. The face-sharing (d), edge-sharing (e), corner-sharing (f), and isolated (g) connectivity of the framework are illustrated. All of the polyhedrons in (d)–(g) represent the polyhedrons of non-lithium cations. The bidirectional arrows in (e) and (f) indicate the unconstrained rotation directions of the connected polyhedrons.*
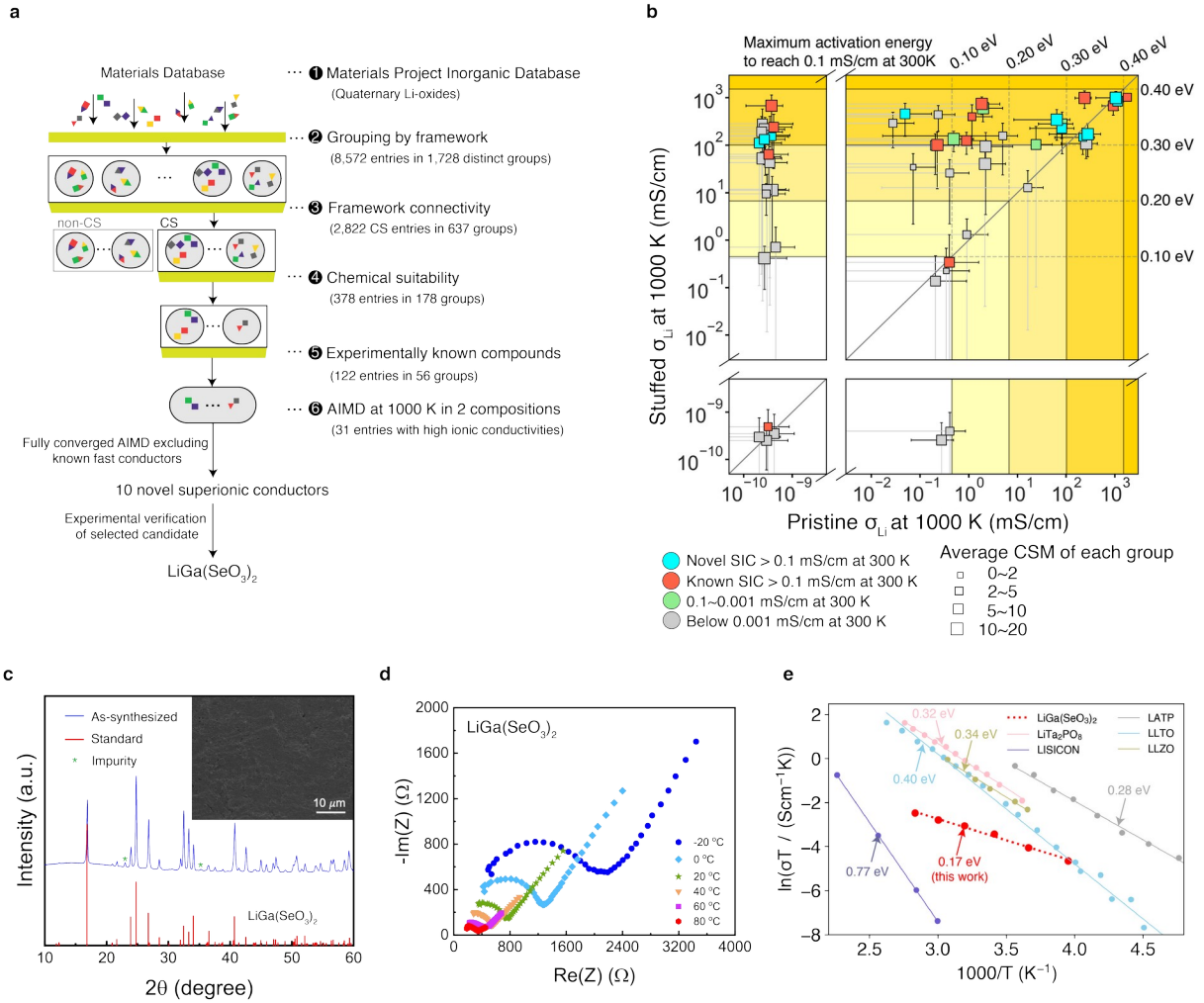
Screening novel superionic conductors with CS frameworks

The CS framework defined above can be used as a structural descriptor to discover other potential Li superionic conductors. To demonstrate this, we perform a multi-step screening process using the Materials Project[38] inorganic crystal structure database starting from 8,572 compounds of quaternary lithium oxides. These are classified into 1,728 distinct structure groups based on the geometry of the framework (anonymizing the *species* of the non-Li

cations) using a structural matching algorithm[39]. By analyzing the connectivity of polyhedrons in these groups, 637 groups with CS frameworks (2,822 compounds) are identified. Compounds with a computed band gap below 2 eV or compounds containing elements unsuitable for solid electrolytes are removed, leaving 378 compounds in 178 groups (see Supplementary Note 1 for details). Finally, only the compounds experimentally reported in the ICSD database[40] are selected for the next screening step, yielding 122 compounds in 56 distinct groups.

At the final screening step, one candidate per structure group is selected for further investigation of its ionic conductivity using AIMD with a target σ_{RT} of 0.1 mS/cm or higher. AIMD simulations are performed at 1000 K for 10 ps for each candidate. Considering that excess lithium via subvalent doping of the stoichiometric phase is often required to achieve high conductivity (Fig. 1a, c and Supplementary Table 2), the AIMD simulations are performed for two compositions for each candidate: the pristine structure (denoted as Pristine) and the structure with one excess Li-ion stuffed into the supercell (denoted as Stuffed). Details are provided in the Methods.

*Figure 2. **Screening for novel superionic conductors with a CS framework and experimental verification of novel superionic conductor LiGa(SeO₃)₂.** (a) Flowchart of the multi-step computational screening and (b) summary of calculated ionic conductivities of 56 materials from Step 6 of (a). The horizontal and vertical lines represent the minimal ionic conductivities at 1000 K required for achieving an extrapolated 0.1 mS/cm at 300 K with correspondingly labeled activation energies. The size of each square represents the average CSM value of each given group. The color represents the classification of each candidate based on its extrapolated ionic conductivity at 300 K. (c) X-ray diffraction pattern of LiGa(SeO₃)₂ with the SEM image of the densified pellet. (d) Temperature-dependent impedance plots of LiGa(SeO₃)₂. The plotted semicircle represents the bulk ionic conductivity. (e) Arrhenius plot of the bulk ionic conductivities in comparison to the bulk ionic conductivities of other oxide superionic conductors.*

In Figure 2b, the AIMD conductivity at 1000 K (σ_{1000K}) of the 56 candidates for two compositions, Pristine and Stuffed, are plotted. Assuming an Arrhenius relationship with 0.3 eV activation energy, which is typical for well-known superionic conductors[16], a value of

9

$\sigma_{1000\,K}$ above 101 mS/cm is required to achieve more than 0.1 mS/cm at room temperature. The minimal $\sigma_{1000\,K}$ for other values of the activation energy (ranging from 0.1 to 0.4 eV) can be found from the vertical (for pristine) and horizontal (for stuffed) solid lines. Only four candidates exhibit negligible ionic conductivity in both the Pristine and Stuffed forms, and eight CS frameworks already exhibit high $\sigma_{1000\,K}$ exceeding 101 mS/cm in the Pristine form. By stuffing a single Li-ion into the supercell, 22 additional CS frameworks can activate high $\sigma_{1000\,K}$ above 101 mS/cm. The orders-of-magnitude improvement of the conductivity upon Li-stuffing cannot be attributed to the quantitative increase of the Li-ion carrier concentration but rather indicates a qualitative change in the energy landscape.

Li stuffing is expected to force lithium into high-energy sites and generate a local group of nearby lithium atoms for which additional Li–Li interaction energy is introduced. Multiple cases where excess lithium stuffing to the stoichiometric phase drastically reduces the activation energy and enhances the ionic conductivity have been reported (Supplementary Table 2). For example, the activation energy of $Li_{1+x}Ta_{1-x}Zr_xSiO_5$[35] (Fig. 1c) decreases from 0.70 eV at the stoichiometric composition to 0.21 eV when the lithium content is increased to x = 0.25. These observations indicate that achieving an optimal lithium concentration is vital to activating fast lithium conduction in CS frameworks. Our sampling of both Pristine and Stuffed compositions captures and corroborates such trends.

Among the 56 CS frameworks (Supplementary Table 3), we rediscover 12 frameworks[29,31] that have been previously reported as lithium superionic conductors (Supplementary Table 1) confirming the selection criteria of our screening process. Among the remaining 44 frameworks, 22 frameworks corresponding to the dark yellow region of Fig. 2b (above the 0.3-eV activation line) exhibit a value of $\sigma_{1000\,K}$ greater than 101.18 mS/cm in either the Pristine or Stuffed composition. On these materials, fully converged multi-temperature AIMD simulation with appropriate subvalent dopants to introduce extra Li are performed. This

10

leads to 10 novel frameworks with conductivity over 0.1 mS/cm at 300 K as summarized in

Table 1. Detailed analysis of the 10 screened conductors is provided in Supplementary Fig.

2–11. Four frameworks with computed ionic conductivity of 0.001–0.1 mS/cm, as well as the

remaining frameworks are summarized in Supplementary Table 4. In total, 22 from the 56

frameworks are demonstrated to exhibit superionic conductivity at RT. The success rate of

39% in screening superionic conductors based on the CS framework largely surpasses that

of random selection[26,27] and other screening studies[31] and indicates that this framework is

indeed a critical structural feature appearing in many existing and potential ionic

conductors.

Table 1. Summary of properties of 10 screened superionic conductors with a CS framework.
The pristine and target composition, extrapolated Li-ion conductivity of the target composition at 300 K ($\sigma_{300\ K}$), activation energy of the target composition (E_a), pristine and target energy above the hull (E_{hull}), and dopant incorporation energy (E_d) are listed. The pristine and target compositions are the same if no dopants are introduced. For conductivity and activation energy, estimation of their upper and lower bounds (error bar) are included.

Materials Project ID	ICSD ID	Pristine composition	Target composition	$\sigma_{300\ K}$ (mS/cm)	E_a (eV)	Pristine E_{hull} (eV/atom)	Target E_{hull} (eV/atom)	E_d (eV/ defect)
mp-1198930	250868	$LiGa(SeO_3)_2$	$LiGa(SeO_3)_2$	0.212 (0.013, 3.57)	0.320 ± 0.070	0.0	0.0	N/A
mp-973966	422056	$LiIn(IO_3)_4$	$LiIn(IO_3)_4$	18.0 (3.57, 90.9)	0.155 ± 0.040	0.0	0.0	N/A
mp-559441	39761	$LiTiPO_5$	$Li_{1+1/16}Ti_{1-1/16}Ga_{1/16}PO_5$	1.70 (0.098, 29.7)	0.212 ± 0.071	0.013	0.019	0.79
mp-14646	65025	$Li_2Mg_2(SO_4)_3$	$Li_{2+1/4}Mg_2(S_{11/12}P_{1/12}O_4)_3$	2.74 (0.145, 52.0)	0.232 ± 0.073	0.0	0.011	0.81
mp-552663	161499	$LiScAs_2O_7$	$Li_{1+3/8}Sc_{1-3/8}Mg_{3/8}As_2O_7$	23.3 (4.26, 128)	0.177 ± 0.042	0.0	0.021	0.64
mp-1020018	428002	$Li_5B(SO_4)_4$	$Li_{5+1/4}B(S_{15/16}P_{1/16}O_4)_4$	0.330 (0.0368, 4.90)	0.330 ± 0.061	0.008	0.023	1.56
mp-1020022	248343	$Li_3B(PO_4)_2$	$Li_{3+1/8}B(P_{15/16}Si_{1/16}O_4)_2$	0.166 (0.00721, 3.83)	0.326 ± 0.078	0.014	0.028	1.63
mp-1020015	192496	$Li_2B_3PO_8$	$Li_{2+1/8}B_3P_{7/8}Si_{1/8}O_8$	0.251 (0.00744, 8.44)	0.269 ± 0.087	0.0	0.015	1.67
mp-1222376	260590	$LiZnBO_3$	$Li_{1+2/16}Zn_{1-1/16}BO_3$	0.605 (0.0104, 35.3)	0.220 ± 0.101	0.008	0.009	0.12
mp-556799	94355	$Li_3In(BO_3)_2$	$Li_{3+1/8}In_{7/8}Zn_{1/8}(BO_3)_2$	0.121 (0.0027, 5.33)	0.300 ± 0.094	0.004	0.009	0.50

Experimental validation of predicted superionic conductors

We pursued $LiGa(SeO_3)_2$ for experimental verification as it does not require excess Li-stuffing

to achieve high conductivity, and is predicted to have a 3-dimensional diffusion channel

which is desirable in solid electrolytes to avoid channel-blocking issues by Li/cation anti-site

11

defects[41] in lower dimensional channels. In addition, the compound has been previously synthesized[42] but was not considered as a lithium ionic conductor. Using a solid-state method, we successfully synthesized $LiGa(SeO_3)_2$ (see Methods). Figure 2c shows the X-ray diffraction (XRD) pattern of the synthesized $LiGa(SeO_3)_2$, which agrees well with its reference pattern except for some small impurity peaks. The pellet was densified using spark plasma sintering (Supplementary Figure 12). While full density was not achieved, the scanning electron microscope (SEM) image in the inset of Fig. 2c shows good connectivity between particles in the densified matrix.

By analyzing the impedance response of a $In/LiGa(SeO_3)_2/In$ Li-blocking cell, we obtained a bulk ionic conductivity of 0.11 mS/cm at 25 °C, which is in excellent agreement with our prediction of 0.21 mS/cm. The electronic conductivity measured at 25ºC in a DC polarization experiment is at least 2 orders of magnitude lower than the ionic conductivity. $LiGa(SeO_3)_2$ also shows a remarkably low bulk activation energy of 0.17 eV, the lowest value among any known oxide Li-ion conductors[18,19,32,33,36] (Fig. 2d). See methods and Supplementary Figure 13-14 for electrochemical analysis. The high ionic conductivity and low activation energy of $LiGa(SeO_3)_2$ validates our prediction that high ionic conductivity can be enabled by corner-sharing frameworks, and encourages further investigation of the predicted materials. The fact that the crystal structure of $LiGa(SeO_3)_2$ has been experimentally known[42] yet never thought to exhibit superionic conductivity demonstrates the predictive power of our high-throughput screening in expanding the currently limited list of oxide superionic conductors.

Origins of fast ionic conduction in CS frameworks: Distortion of Li sites

To reveal the physical origin of the high ionic conductivity in the CS frameworks, we take a two-track strategy by systematically investigating both the individual Li-site geometry as well as their relationship with the framework. We compare the lithium coordination environments in 2,822 compounds with CS frameworks (637 groups) to those in 5,750 compounds with non-CS frameworks (1,091 groups) by calculating the Continuous

12

Symmetry Measure[43] (CSM) where a minimum of 0 corresponds to a perfectly symmetric coordination environment and the maximum of 66.7 corresponds to infinite elongation along one direction[44] (Supplementary Note 2).

Figure 3 compares the CSM values of octahedral and tetrahedral lithium environments in CS and non-CS frameworks including both occupied and unoccupied lithium sites for each framework. We find that the CS frameworks generally provide a much wider range of degree of distortion in lithium sites, similar to our observations for the three CS superionic conductors in Fig. 1. The CSM values of tetrahedral and octahedral sites of the CS frameworks are evenly distributed up to a value as high as 15, indicating that the Li-ions are frequently accessing highly distorted environments. However, most of the non-CS frameworks have CSM values near 0, indicating a high propensity for a non-CS framework to provide a highly symmetric environment. Therefore, our analysis indicates that symmetric tetrahedral and octahedral sites are much less frequently provided in CS frameworks. Supplementary Fig. 15-16 provide details of the same set of data with the occupied and unoccupied lithium sites separately analyzed, revealing the same trend. Details are provided in the Methods section and Supplementary Note 3.

13
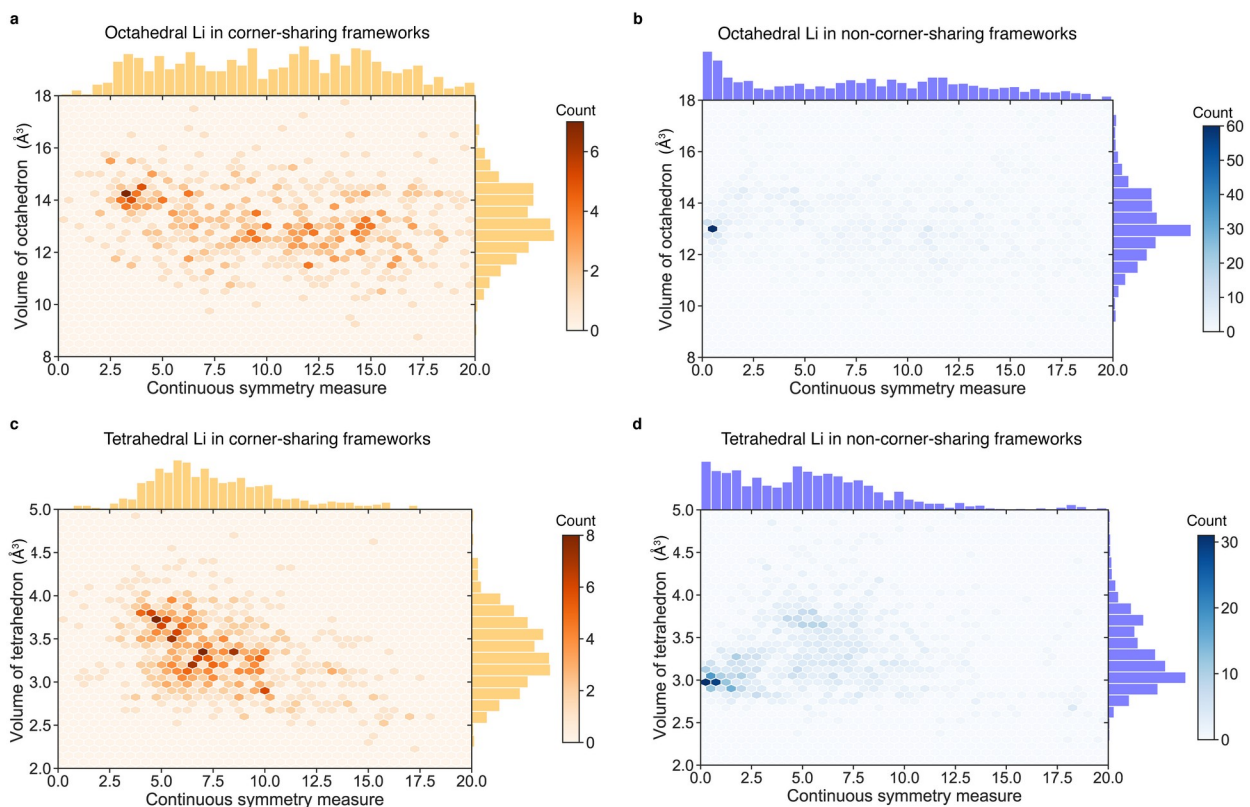
Figure 3. **Lithium environment in oxide materials with 2,822 CS and 5,750 non-CS frameworks.** *The octahedral lithium environment for CS (a) and non-CS frameworks (b), and tetrahedral lithium environment for CS (c) and non-CS frameworks (d). The color intensities indicate the number of entries that are populated in a given hexagon. These analyses include both the occupied and unoccupied lithium sites.*

The high distortion of lithium sites in structures with a CS framework can be understood from the geometry of the framework polyhedrons. Although lithium can accommodate various extents of distortion, the non-Li polyhedrons that build up the framework are nearly perfectly symmetric (Supplementary Fig. 17). This is attributed to the highly covalent nature of bonding in the polyhedra (PO_4, SiO_4, SO_4) or the lower ionic nature of non-Li metal polyhedrons (Mg-octahedron, Ta-octahedron, Al-tetrahedron) compared to lithium. In contrast, the Li–O bond has a highly ionic nature because lithium's low electronegativity limits the degree of hybridization with the oxygen atom. Therefore, the equilibrium crystal structures prioritize the formation of perfectly symmetric framework polyhedra over a symmetric Li environment. Furthermore, the degree of freedom for the relative positioning of two adjacent non-Li polyhedrons significantly increases as less oxygen anions are shared

14

between them, as illustrated in Fig. 1d-g. The higher freedom in the arrangement of the framework polyhedrons leads to a more irregular geometry of its interstitial space, explaining why CS frameworks tend to have lithium environments with notably larger distortion. We note that a perfectly symmetric lithium environment is not necessarily prohibited in a CS framework, as observed in the perfect tetrahedral lithium sites in corner-sharing LISICON frameworks (Supplementary Fig. 1). Rather, the CS framework allows for a wide range of CSM values, which includes everything from perfect to highly distorted environments.

The distorted lithium sites in CS frameworks are the key to achieving a Li-ion energy landscape with low migration energy. Li-ions have higher energy in the distorted sites than in the symmetric ones. Therefore, migration of lithium from a distorted coordination environment within a CS framework results in a reduction of its activation energy, as illustrated in Fig. 4a. To illustrate the effectiveness of lithium site distortion in enhancing the ionic conductivity, we calculate the kinetically resolved activation energy[45] (E_{KRA}) for lithium migration in model structures with different levels of distortion. E_{KRA} is used to remove the effect of site energy difference on the overall activation energy and solely probes the effect of distortion of the initial site on the migration energy while being independent of the energy state of the final site. To continuously sample a wide range of lithium environments, we trace a Bain path which is a distortion trajectory that connects a bcc anion lattice to an fcc anion lattice and evaluate the Li migration energy for different polyhedral volumes, as shown in Fig. 4b. This path enables us to continuously evaluate the effect of distortion on the Li migration barrier, starting from a perfectly symmetric lithium environment in an fcc anion framework and reaching highly distorted environments as larger strains are applied. Details are provided in the Methods section.
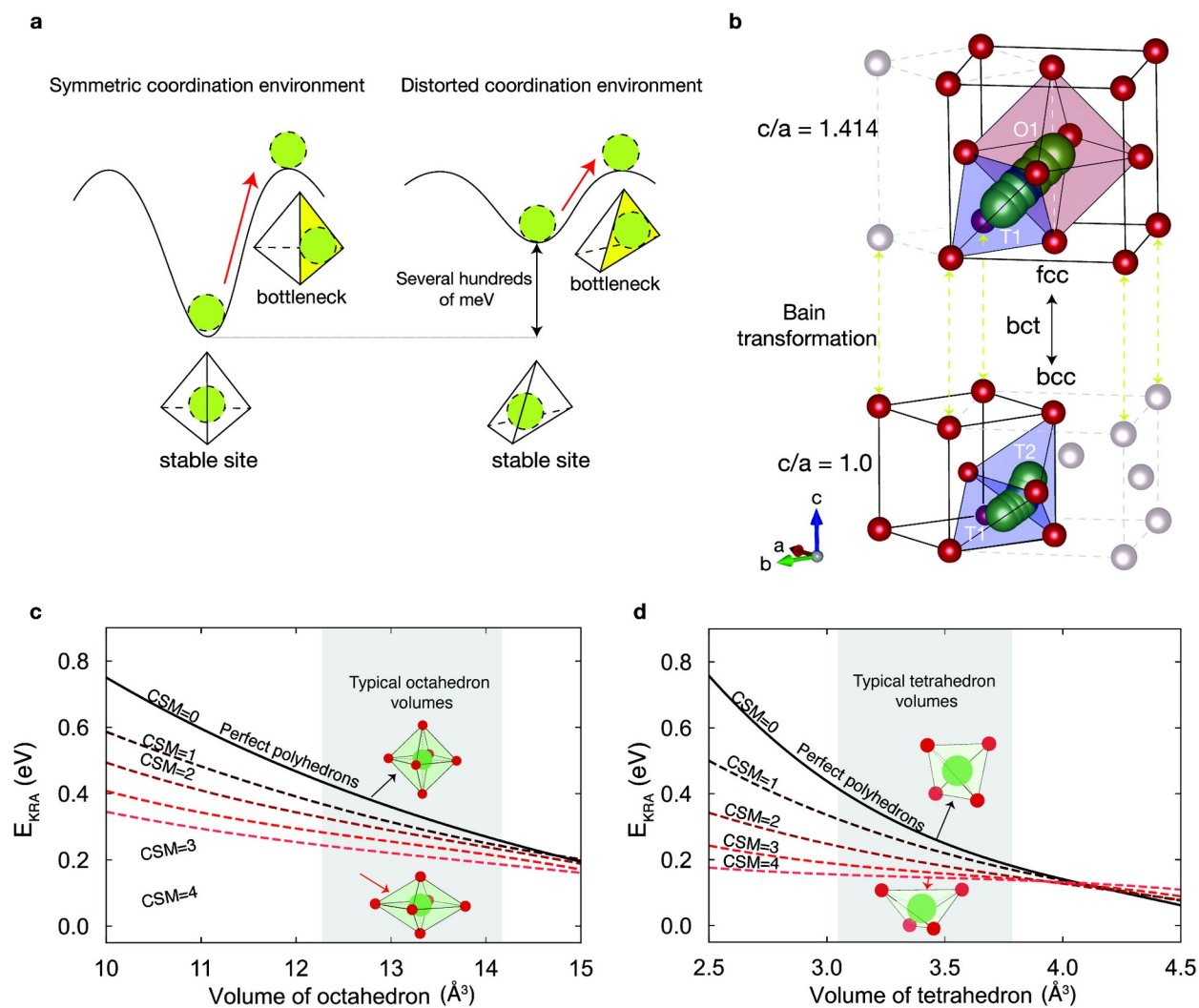
*Figure 4. **Effect of distorted lithium environment on the energy landscape.** (a) The distortion of the lithium environment leads to the destabilization of lithium sites and reduces the energy gap to the transition state. (b) The lithium activation in a wide range of coordination environments is evaluated using model structures along the path of Bain transformation. The shaded triangular face is the bottleneck for lithium migration from its initial site. The lithium and oxygen atoms are shown as green and red (beige if outside the unit cell) circles, respectively. Calculated Li-ion kinetically resolved activation energies (E_{KRA}) in these model systems are shown for both octahedral (c) and tetrahedral (d) sites ranging from CSM = 0 (perfect polyhedrons) to CSM = 4. Typical octahedral and tetrahedral volumes from our lithium environment analysis explained in the Methods are shown in shades.*

Figure 4c-d shows the calculated E_{KRA} as a function of polyhedral volume for a series of CSM values from 0 (perfect polyhedrons) to CSM = 4 (significant distortion). We find that throughout the typical volume ranges of Li polyhedrons, E_{KRA} decreases by as much as several hundreds of meV with increasing distortion of the Li polyhedrons. Our calculations

17

clearly demonstrate that distorting the lithium sites raise their site energies and reduce the energy gap to the transition state, leading to higher ionic conductivity. The effect of the polyhedral volume on the migration barrier is more complicated with the barrier generally increasing for a smaller polyhedron except for the most distorted polyhedron. The results here align with our previous work[20] and provide a different perspective on the low activation barrier in materials with a bcc anion lattice where the tetrahedral sites are naturally distorted with a CSM value of 2.3 even for the perfect bcc geometry. Our analysis is also aligned with recent work[29,31,43] that notes the distortion of the anion lattice in superionic conductors.

Origins of fast ionic conduction in CS frameworks: Reduced cation interactions

We now demonstrate that the arrangement of the Li sites within the structure of CS frameworks also promotes fast ionic motion. We define the polyhedral packing ratio as: $\alpha = \frac{Volume\ of\ framework\ polyhedrons}{Volume\ of\ unit-cell}$. Figure 5a shows that CS frameworks have a significantly lower polyhedral packing ratio than non-CS frameworks. This allows a large fraction of lithium sites to be distant from non-Li cations and reduces the electrostatic repulsion from them. Specifically, Figure 5b compares the likelihood of a lithium site being distant from any non-Li cations. The site ratio β is defined as: $\frac{Distant\ Li\ sites}{Total\ available\ Li\ sites}$ where *Distant Li-sites* count the number of Li-sites that do not have any non-Li cations within the cutoff distance of 1.95 Å; for shorter distances than the cutoff, any lithium will form a face-sharing connection with adjacent framework polyhedra (see Methods). The β ratio is significantly higher for the CS framework, indicating that they have a much higher proportion of Li sites that are not face-sharing with the framework polyhedrons and experience reduced electrostatic interaction from the non-Li cations.

18
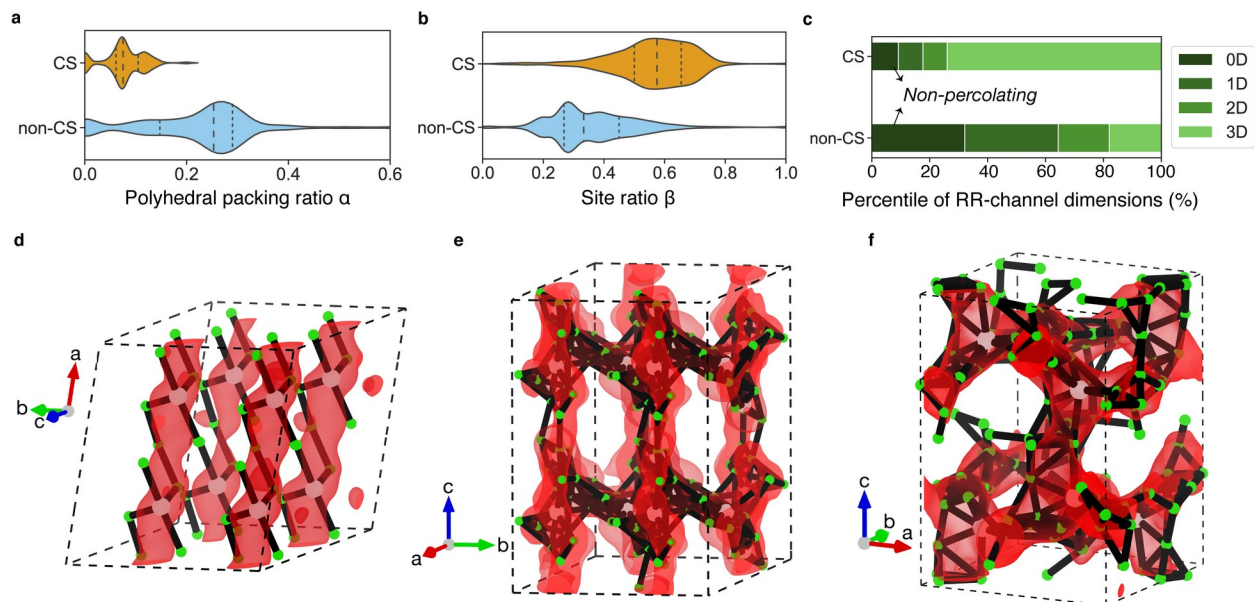
Figure 5. **Structural features of CS framework and their RR-channels**. *Comparison of the polyhedral packing ratio α (a), site ratio β (b), and dimension of RR-channel of CS and non-CS frameworks (c). The RR-channels (solid black lines) in three screened conductors with CS frameworks, $LiScAs_2O_7$ (d), $Li_3B(PO_4)_2$ (e), and $Li_2Mg_2(SO_4)_3$ (f), are shown together with the lithium probability densities from AIMD simulations (red isosurfaces). Isosurfaces are shown in red at $P_0/100$ (d), $P_0/1000$ (e), and $P_0/1000$ (f), where P_0 is the maximum value of the probability density. The RR-channels are shown as connected black edges. The green and white spheres represent occupied and unoccupied lithium sites, respectively, in each crystal structure.*

Here, we define a reduced-repulsion (RR) channel as a percolating channel of *Distant Li-sites (see Methods)*. By following the RR-channel, Li-ions minimize the interaction with non-Li cations and travel through a relatively flat energy landscape. We show in Fig. 5d-f for three examples from the screened candidates that the RR-channels match well the actual Li diffusion pathways obtained from AIMD simulations. Considering the weaker screening ability of oxygen anions and the pronounced effect of the arrangement of non-Li cations on lithium diffusion, RR-channels should play a more critical role in oxide conductors than in sulfide conductors. We also find that the CS frameworks are more likely to form high-dimensional RR-channels. Figure 5c shows that while over 75% of the CS frameworks have a 3D RR-channel, more than 75% of the non-CS frameworks have lower-dimension RR-channels. Materials with low-dimensional diffusion channels, especially 1D, may have limited macroscopic conductivity because of the detrimental effect of channel-blocking defects[41].

19

The advantage of CS frameworks can be demonstrated in an exemplary way by taking two compounds ($LiSbP_2O_7$ and $LiNbWO_6$) which can form in both a CS and non-CS polymorph. We find that while the non-CS frameworks exhibit either poor or non-existing Li-motion in AIMD simulations, the CS polymorphs provide fast lithium transport (See detailed analysis in Supplementary Note 4). We note that, the similar definition of percolating 0-TM channels in disordered rocksalt cathode materials[46] is actually a subset of our definition of RR-channels here. When lithium follows an *oct–tet–oct* path, as in closed-packed oxides, its migration energy is the lowest when the intermediate tetrahedral site face-shares with no transition metals (0-TM channels).

In addition to the two aforementioned advantages, the flexible nature of the corner-sharing connectivity can promote Li migration by facilitating relaxation of the framework to accommodate the Li-ion passing through the bottleneck. As more anions are shared between adjacent cation polyhedrons, the flexibility of the framework to relax during a Li-migration event decreases. While face-sharing connectivity requires at least three commonly shared anions, CS structures have at most one common anion vertex being shared between adjacent cation polyhedrons. This loose restriction on the framework connectivity provides a large degree of freedom for the framework polyhedrons to relax (e.g., rotation) and give way for the migrating Li-ion. The rotation of framework polyhedrons in Li[47,48], Na[49] and Mg[50] ion conductors is an example of the facile relaxation allowed in CS frameworks.

Other oxide superionic conductors with large rare-earth cations such as garnets and perovskites do not have CS frameworks because of their large La polyhedrons, but the origin of their high ionic conductivity can be well understood using similar structural features. The structure of garnet $Li_7La_3Zr_2O_{12}$ is built from large 8-coordinated La polyhedrons edge-shared among themselves, and Zr octahedrons. Throughout the *tet–oct–tet* channel connecting 24d and 96h sites, the minimum distance between any lithium site and its nearest Zr or La site in

20

a garnet is 2.95 Å (Supplementary Note 5). Although the octahedral (96h) Li site face-shares with the La polyhedrons, the distance between them is 3.07 Å, significantly larger than typical face-sharing distances. Therefore, the *tet–oct–tet* pathways in garnet structures are indeed RR-channels. Similar argument can be made for perovskites (Supplementary Note 6). Therefore, although these frameworks form edge / face-sharing connections, the presence of large La cations in garnet and perovskite creates sufficient space to make the Li pathway a RR-channel. Furthermore, the Li environment in the off-symmetric A site of perovskite can be classified as a highly distorted octahedral site with a CSM value of 16.5–17.4. The fact that the perovskite structure does not provide any regular tetrahedral or octahedral Li site suggests its high similarity to the CS frameworks.

In summary, our study highlights corner-sharing framework as an important structural feature of a large class of lithium superionic conductors. The fast diffusion of lithium in such CS frameworks is rationalized by the distorted Li site environments these structures create, and from their low polyhedral density creating well-connected RR-channels, which minimize electrostatic repulsion from non-Li cations as Li-ions travel through them. The strong predictive power of the CS structural descriptor was demonstrated in a high-throughput screening, leading to the discovery of 10 novel frameworks with high computed conductivity. Among them, $LiGa(SeO_3)_2$ was experimentally verified as a novel superionic conductor with low activation energy. Our findings provide fundamental insights in the physical attributes that allow fast lithium conduction and project an exciting direction toward the accelerated discovery of superionic conductors for all-solid-state batteries.

21

Author Contributions

Y.W. initially proposed the concept. K.J. carried out all of the calculations with the help of Y.X. Y.X. implemented the site identifying algorithm. Y.S. synthesized the conductor. Y.S., Y.Z., and R.K. densified the pellet. Y.S. performed the electrochemical characterization and analyzed them with Y.Z., K.J., H.K. and L.J.M. G.C., Y.W. and D.I. supervised the project. K.J., Y.S., Y.W. and G.C. wrote the manuscript with contribution and revisions from all authors.

Declaration of Interests

Patent applications have been filed on some of the discovered Li superionic conductor structures and compositions.

Methods

Identifying Li sites in crystal structures

The algorithm to identify occupied and unoccupied Li sites in a crystalline Li oxide is described in Supplementary Fig. 18. A Delaunay tetrahedralization algorithm[51] was used on the O^{2-} anion lattice to generate "***T*** tetrahedral sites" (***T*** sites). For each existing Li ion, a "Li polyhedral site" (***L*** sites) was constructed by finding its coordinating anions (cutoff distance ≤ 3 Å), and similar for "***M*** polyhedral sites" (***M*** sites) for each non-Li (M) cation. Two sites were defined to be "in conflict" with each other if their center distance ≤ 1 Å. Next, any ***T***

sites that were "in conflict" with any **M** sites were removed, and the remaining **T** sites were recursively merged if they were both distorted (Robert/Roux factor ≤ 0.94)[52] and too close to each another (center distance ≤ 1.1 Å). This step produced "candidate polyhedral sites" (**P** sites) consisting of the unmerged **T** sites and also the new sites from merging. Finally, we designated any **P** sites that were "in conflict" with any **L** sites as the occupied Li sites and the remaining **P** sites as the unoccupied Li sites. All numerical values were selected to reproduce the known Li sites in experimentally identified structures, including garnet, NASICON, layered $LiCoO_2$ and spinel $LiMn_2O_4$. In the newly predicted structures, stuffed lithium was inserted in the lowest energy site according to DFT calculations.

Coordination environments in CS and non-CS frameworks

Two CSM values of each Li site were calculated referencing to a perfect tetrahedron and a perfect octahedron, and denoted as CSM_{tet} and CSM_{oct}, respectively. The site was then assigned as a tetrahedral site if CSM_{tet} was smaller than CSM_{oct} (*i.e.,* the site was geometrically closer to a perfect tetrahedron than to a perfect octahedron) and vice versa (see Supplementary Note 3). To remove the bias in our dataset towards fcc anion frameworks resulting from extensive experimental studies on cathode materials, all the structures were grouped by the geometry of their frameworks using a structural matching algorithm[39]. A representative structure was randomly selected from each group. CSM_{tet} and CSM_{oct} values were averaged over all tetrahedral and octahedral Li sites in the structure, respectively, to represent the coordination environments in the group.

Phase stability of compounds with aliovalent dopants

Density functional theory calculations were performed with the Perdew–Burke–Ernzerhof (PBE) generalized gradient approximation[53] (GGA) using the projector augmented wave (PAW) method[54] as implemented in the Vienna ab initio simulation package (VASP)[55]. A mixed scheme of the GGA and GGA+U methods was used [56], and the selection of *k*-point grid and energy cutoff was consistent with the computational settings in the Materials

23

Project[38]. The phase stability of each compound was evaluated by generating the convex hull formed by the ground-state phases in the chemical space defined by all of the elements in the material including the dopant species using the pymatgen software package[39]. Materials above the convex hull are expected to decompose into their nearest phase on the facet of the convex hull. The energy above the hull as well as the dopant (defect) incorporation energy were calculated to evaluate the stability of the doped compound. The dopant incorporation energy was calculated as[57]: $E_d = E\square_{doped} - E_{pristine} + \sum_i \Delta n_i \mu \square_i$ where E_{doped} and $E_{pristine}$ are the DFT energies of the supercells with and without dopants, μ_i is the chemical potential of the element i on the convex hull and Δn_i is the change in the number of atoms of element i in the supercell to introduce the dopants.

Li site distortion and its effect on Li migration barrier

Bcc anion frameworks with volumes between 10 $\text{Å}^3/\text{O}$ and 35 $\text{Å}^3/\text{O}$ at an interval of 1 $\text{Å}^3/\text{O}$ were generated covering the typical volume range of the tetrahedral and octahedral Li sites in the Li oxides, as shown in Fig. 3. To sample various degrees of distortion of lithium environments, a Bain transformation was applied by elongating the c-axis from c/a = 0.4 to c/a = 1.7 at an interval of 0.05. Structures with c/a values that are not 1.0 (bcc) or 1.414 (fcc) have body-centered-tetragonal (bct) anion frameworks. E_{KRA} was calculated from the site energies of T1 site, T2 or O1 site, and the planar triangular bottleneck using DFT structure optimization. The discrete results at various distortions and volumes were interpolated to obtain the E_{KRA} as a function of CSM and volume per polyhedron. Sample points where the Li placed at the O1 site escapes from the octahedral site after relaxation were excluded.

Identification of RR-channel

In computing the site ratio β and identifying the RR-channels, we searched for Li sites that have no non-Li cations within a radius of 1.95 Å. This cutoff distance between a Li site and

24

its nearest non-Li cation was chosen to set the boundary between a corner- or edge-sharing connectivity and a face-sharing connectivity. A typical Li–non-Li cation of a corner- or edge-sharing connectivity is larger than 1.95 Å whereas that of a face-sharing connectivity is smaller than 1.95 Å. For example, the distance between the edge-sharing P and Li polyhedrons is 2.69 Å in LiFePO$_4$, that of a corner-sharing Zr–Li connection is 2.94 Å in LLZO, and that of a corner-sharing Li–Mn is 3.49 Å in spinel LiMn$_2$O$_4$. In contrast, the distance between an octahedral site and a face-sharing activated tetrahedral site in lithium disordered rocksalt is 1.79 Å[46]. We identify RR-channels by connecting nearby lithium sites within 2.3 Å and determine the dimensionality of the RR-channels by evaluating their percolation in the crystal structure

Ab-initio molecular dynamics simulations

AIMD simulations were performed using gamma-point-only sampling of k-space and a plane-wave energy cutoff of 520 eV. Spin polarized calculations were performed if magnetic moment appeared during the DFT total energy calculation. In the short AIMD of Li-stuffed compounds, a background charge was applied to retain the oxidation states of the framework atoms. For both the short AIMD simulation and the fully converged AIMD simulation, the samples were heated to the target temperature over 2 ps using velocity scaling, and then were equilibrated at the target temperature for 5 ps in the NVT ensemble using a Nosé–Hoover thermostat. For the short AIMD, we then performed the simulation for diffusion in the NVT ensemble for 10 ps. For the fully converged AIMD simulation of the 10 novel superionic conductors, we sampled diffusion events for 100–500 ps per temperature in the NVT ensemble until the diffusion coefficient converged. For each compound, at least 5 temperatures were simulated for the linear fitting of the Arrhenius relationship. The diffusion coefficient was evaluated using the mean squared displacement based on the methodology established in previous works[23]. The lithium ionic conductivity was calculated from the diffusion coefficient based on the Einstein's relation. No signs of melting at high temperature were observed. Error analysis was performed based on the empirical relationship between

25

the total mean squared displacement and the relative standard deviation (RSD) of the diffusion coefficient[58]. In a few cases with insufficient number of hopping events, the lower limit of the error bar was drawn in light grey arbitrarily down to 1/1000 of the computed conductivity from the 10-ps AIMD simulation.

Synthesis

$LiGa(SeO_3)_2$ was synthesized via a solid state method. 0.2096 g lithium carbonate (Li_2CO_3, Sigma-Aldrich, 99.99% trace metal basis), 0.5316 g gallium (III) oxide (Ga_2O_3, Sigma-Aldrich, >99.99 trace metal basis) and 1.2588 g selenium dioxide (SeO_2, Sigma-Aldrich, >99.9 trace metal basis) were mixed in the appropriate stoichiometric ratio. The mixtures were hand ground in an agate mortar for 15 mins and transferred into a zirconium oxide ball mill jar together with 2 large zirconium oxide balls (10 mm in diameter) and 25 small zirconium oxide balls (5 mm in diameter). The mixture was then ball milled (SpexSamplePrep 8000M) for 1 hours. After ball milling, the mixture was pressed into pellets of 6.0 mm in diameter under a pressure of 2.0 metric tons for 4 mins. The pellets were put into an alumina combustion boat and calcined at 310°C for 48 hours under argon flow to obtain $LiGa(SeO_3)_2$. All the experimental procedures are carried out in an argon atmosphere with <0.1 ppm of O_2 and H_2O.

Electrochemical characterization

The Li-ion conductivity was evaluated using electrochemical impedance spectroscopy (EIS) with Indium metal as blocking electrodes at temperature ranging from -20°C to 80°C. As-synthesized $LiGa(SeO_3)_2$ is sintered to a ~1-mm-thick pellet with a diameter of 12.7 mm via Spark Plasma Sintering (Thermal Technology LLC, Model DCS25). LiCl (3 wt.%) is used as a sintering additive. During the sintering, the powder was uniaxially compressed using a WC-6% Co press die under a pressure of 160 MPa at 300°C. The as-obtained pellet was then sandwiched between two Indium films and transferred into Bio-Logic leak-tight sample holders (CESH) for EIS measurements. EIS measurements were performed using an EC-Lab

26

Electrochemistry, SP300, Bio-Logic. The measurements were conducted at the initial open-circuit voltage in the frequency range of 7 MHz to 100 mHz with the application of a 10-mV signal amplitude. A Bio-Logic intermediate temperature system (ITS) was used to control the temperature of the sample holder. The electronic conductivity was evaluated using direct current (DC) polarization test. A 20 mV DC voltage was applied on the In/LiGa(SeO$_3$)$_2$/In cell.

Structural characterization

Powder XRD data was collected using a Rigaku MiniFlex 600 diffractometer with Cu K_α radiation. SEM images were obtained on a Zeiss Gemini Ultra-55 analytical field-emission scanning electron microscope at the Molecular Foundry at Lawrence Berkeley National Laboratory (LBNL).

References

1   Schmuch, R., Wagner, R., Hörpel, G., Placke, T. & Winter, M. Performance and cost of materials for lithium-based rechargeable automotive batteries. *Nature Energy* **3**, 267-278, doi:10.1038/s41560-018-0107-2 (2018).

2   Randau, S. *et al.* Benchmarking the performance of all-solid-state lithium batteries. *Nature Energy*, 1-12, doi:10.1038/s41560-020-0565-1 (2020).

3   Famprikis, T., Canepa, P., Dawson, J. A., Islam, M. S. & Masquelier, C. Fundamentals of inorganic solid-state electrolytes for batteries. *Nature Materials*, 1-14, doi:10.1038/s41563-019-0431-3 (2019).

4   Nam, Y. J., Oh, D. Y., Jung, S. H. & Jung, Y. S. Toward practical all-solid-state lithium-ion batteries with high energy density and safety: Comparative study for electrodes fabricated by dry- and slurry-mixing processes. *J Power Sources* **375**, 93-101, doi:10.1016/j.jpowsour.2017.11.031 (2018).

5   Barroso-Luque, L., Tu, Q. & Ceder, G. An Analysis of Solid-State Electrodeposition-Induced Metal Plastic Flow and Predictions of Stress States in Solid Ionic Conductor Defects. *J Electrochem Soc* **167**, 020534, doi:10.1149/1945-7111/ab6c5b (2020).

6   Kamaya, N. *et al.* A lithium superionic conductor. *Nat Mater* **10**, 682-686, doi:10.1038/nmat3066 PMID - 21804556 (2011).

7   Seino, Y., Ota, T., Takada, K., Hayashi, A. & Tatsumisago, M. A sulphide lithium super ion conductor is superior to liquid ion conductors for use in rechargeable batteries. *Energy Environ Sci* **7**, 627-631, doi:10.1039/c3ee41655k (2014).

8   Zhou, L., Assoud, A., Zhang, Q., Wu, X. & Nazar, L. F. New Family of Argyrodite Thioantimonate Lithium Superionic Conductors. *J Am Chem Soc* **141**, 19002-19013, doi:10.1021/jacs.9b08357 PMID - 31642663 (2019).

9   Yamane, H. *et al.* Crystal structure of a superionic conductor, Li7P3S11. *Solid State Ionics* **178**, 1163-1167, doi:10.1016/j.ssi.2007.05.020 (2007).

10   Richards, W. D., Miara, L. J., Wang, Y., Kim, J. C. & Ceder, G. Interface Stability in Solid-State Batteries. *Chemistry of Materials* **28**, 266-273, doi:10.1021/acs.chemmater.5b04082 (2016).

11   Xiao, Y. *et al.* Understanding interface stability in solid-state batteries. *Nat Rev Mater*, 1-22, doi:10.1038/s41578-019-0157-5 (2019).

12   Wood, K. N. *et al.* Operando X-ray photoelectron spectroscopy of solid electrolyte interphase formation and evolution in Li2S-P2S5 solid-state electrolytes. *Nat Commun* **9**, 2490, doi:10.1038/s41467-018-04762-z PMID - 29950672 (2018).

13   Wenzel, S. *et al.* Direct Observation of the Interfacial Instability of the Fast Ionic Conductor Li10GeP2S12 at the Lithium Metal Anode. *Chemistry of Materials* **28**, 2400-2407, doi:10.1021/acs.chemmater.6b00610 (2016).

14   Lian, P.-J. *et al.* Inorganic sulfide solid electrolytes for all-solid-state lithium secondary batteries. *J Mater Chem A* **7**, 20540-20557, doi:10.1039/c9ta04555d (2019).

15   Xu, X. *et al.* Li7P3S11 solid electrolyte coating silicon for high-performance lithium-ion batteries. *Electrochim Acta* **276**, 325-332, doi:10.1016/j.electacta.2018.04.208 (2018).

16   Zhang, Z. *et al.* New horizons for inorganic solid state ion conductors. *Energy & Environmental Science* **11**, 1945-1976, doi:10.1039/c8ee01053f (2018).

17   Aono, H. Ionic Conductivity of Solid Electrolytes Based on Lithium Titanium Phosphate. *J Electrochem Soc* **137**, 1023, doi:10.1149/1.2086597 (1990).

18   Murugan, R., Thangadurai, V. & Weppner, W. Fast Lithium Ion Conduction in Garnet-Type Li7La3Zr2O12. *Angewandte Chemie International Edition* **46**, 7778-7781, doi:10.1002/anie.200701144 PMID - 17803180 (2007).

19   Stramare, S., Thangadurai, V. & Weppner, W. Lithium Lanthanum Titanates: A Review. *Chemistry of Materials* **15**, 3974-3990, doi:10.1021/cm0300516 (2003).

20   Wang, Y. *et al.* Design principles for solid-state lithium superionic conductors. *Nat Mater* **14**, 1026-1031, doi:10.1038/nmat4369 PMID - 26280225 (2015).

21   Richards, W. D., Wang, Y., Miara, L. J., Kim, J. C. & Ceder, G. Design of Li 1+2x Zn 1−x PS 4 , a new lithium ion conductor. *Energ Environ Sci* **9**, 3272-3278, doi:10.1039/c6ee02094a (2016).

22   Suzuki, N. *et al.* Synthesis and electrochemical properties of I‾4 type Li1+2xZn1-xPS4 solid electrolyte. *Chemistry of Materials*, doi:10.1021/acs.chemmater.7b03833 (2018).

23   Ong, S. P. *et al.* Phase stability, electrochemical stability and ionic conductivity of the Li 10±1 MP 2 X 12 (M = Ge, Si, Sn, Al or P, and X = O, S or Se) family of superionic conductors. *Energ Environ Sci* **6**, 148-156, doi:10.1039/c2ee23355j (2012).

24   Kanno, R., Hata, T., Kawamoto, Y. & Irie, M. Synthesis of a new lithium ionic conductor, thio-LISICON–lithium germanium sulfide system. *Solid State Ionics* **130**, 97-104, doi:10.1016/s0167-2738(00)00277-0 (2000).

25   Knauth, P. Inorganic solid Li ion conductors: An overview. *Solid State Ionics* **180**, 911-916, doi:10.1016/j.ssi.2009.03.022 (2009).

26   Sendek, A. D. *et al.* Holistic computational structure screening of more than 12000 candidates for solid lithium-ion conductor materials. *Energ Environ Sci* **10**, 306-320, doi:10.1039/c6ee02697d (2016).

27   Sendek, A. D. *et al.* Machine Learning-Assisted Discovery of Solid Li-Ion Conducting Materials. *Chemistry of Materials* **31**, 342-352, doi:10.1021/acs.chemmater.8b03272 (2018).

28   Muy, S. *et al.* High-throughput screening of solid-state Li-ion conductors using lattice-dynamics descriptors. *iScience* **16**, 270-282, doi:10.1016/j.isci.2019.05.036 PMID - 31203184 (2019).

29   Zhang, Y. *et al.* Unsupervised discovery of solid-state lithium ion conductors. *Nature Communications* **10**, 5260, doi:10.1038/s41467-019-13214-1 (2019).

30   Kahle, L., Marcolongo, A. & Marzari, N. High-throughput computational screening for solid-state Li-ion conductors. *Energy & Environmental Science*, doi:10.1039/c9ee02457c (2020).

31   He, X. *et al.* Crystal Structural Framework of Lithium Super-Ionic Conductors. *Adv Energy Mater*, 1902078, doi:10.1002/aenm.201902078 (2019).

32   Arbi, K., Mandal, S., Rojo, J. M. & Sanz, J. Dependence of Ionic Conductivity on Composition of Fast Ionic Conductors Li1+xTi2-xAlx(PO4)3, 0 ≤ x ≤ 0.7. A Parallel NMR and Electric Impedance Study. *Chemistry of Materials* **14**, 1091-1097, doi:10.1021/cm010528i (2002).

33   Kim, J., Kim, J., Avdeev, M., Yun, H. & Kim, S.-J. LiTa 2 PO 8 : a fast lithium-ion conductor with new framework structure. *J Mater Chem A* **6**, 22478-22482, doi:10.1039/c8ta09170f (2018).

34   Wang, Q. *et al.* A New Lithium-Ion Conductor LiTaSiO5: Theoretical Prediction, Materials Synthesis, and Ionic Conductivity. *Adv Funct Mater* **29**, 1904232, doi:10.1002/adfm.201904232 (2019).

35   Xiong, S. *et al.* Computation-Guided Design of LiTaSiO5, a New Lithium Ionic Conductor with Sphene Structure. *Adv Energy Mater* **9**, 1803821, doi:10.1002/aenm.201803821 (2019).

36   Hong, H. Y. P. Crystal structure and ionic conductivity of Li14Zn(GeO4)4 and other new Li+ superionic conductors. *Mater Res Bull* **13**, 117-124, doi:10.1016/0025-5408(78)90075-2 (1978).

37   Bruce, P. G. & West, A. R. Phase diagram of the LISICON, solid electrolyte system, Li4GeO4 Zn2GeO4. *Mater Res Bull* **15**, 379-385, doi:10.1016/0025-5408(80)90182-8 (1980).

38   Jain, A. *et al.* Commentary: The Materials Project: A materials genome approach to accelerating materials innovation. *Apl Mater* **1**, 011002, doi:10.1063/1.4812323 (2013).

39   Ong, S. P. *et al.* Python Materials Genomics (pymatgen): A robust, open-source python library for materials analysis. *Comp Mater Sci* **68**, 314-319, doi:10.1016/j.commatsci.2012.10.028 (2013).

40   Belsky, A., Hellenbrandt, M., Karen, V. L. & Luksch, P. New developments in the Inorganic Crystal Structure Database (ICSD): accessibility in support of materials research and design. *Acta Crystallographica Section B: Structural Science* **58**, doi:10.1107/s0108768102006948 PMID - 12037357 (2002).

41   Malik, R., Burch, D., Bazant, M. & Ceder, G. Particle Size Dependence of the Ionic Diffusivity. *Nano Letters* **10**, 4123-4127, doi:10.1021/nl1023595 PMID - 20795627 (2010).

42   Lee, D. W. & Ok, K. M. New Alkali-Metal Gallium Selenites, AGa(SeO3)2 (A = Li, Na, K, and Cs): Effect of Cation Size on the Framework Structures and Macroscopic Centricities. *Inorg Chem* **52**, 5176-5184, doi:10.1021/ic400458a PMID - 23590567 (2013).

43   Stefano, D. D. *et al.* Superionic Diffusion through Frustrated Energy Landscape. *Chem*, doi:10.1016/j.chempr.2019.07.001 (2019).

44   Pinsky, M. & Avnir, D. Continuous Symmetry Measures. 5. The Classical Polyhedra. *Inorg Chem* **37**, 5575-5582, doi:10.1021/ic9804925 PMID - 11670704 (1998).

45   Ven, A. V. d., Ceder, G., Asta, M. & Tepesch, P. D. First-principles theory of ionic diffusion with nondilute carriers. *Phys Rev B* **64**, 184307, doi:10.1103/physrevb.64.184307 (2001).

46   Lee, J. *et al.* Unlocking the Potential of Cation-Disordered Oxides for Rechargeable Lithium Batteries. *Science* **343**, 519-522, doi:10.1126/science.1246432 PMID - 24407480 (2014).

47   Zhang, Z. *et al.* Targeting Superionic Conductivity by Turning on Anion Rotation at Room Temperature in Fast Ion Conductors. *Matter* **2**, 1667-1684, doi:10.1016/j.matt.2020.04.027 (2020).

48   Hanghofer, I., Gadermaier, B. & Wilkening, H. M. R. Fast Rotational Dynamics in Argyrodite-Type Li 6 PS 5 X (X: Cl, Br, I) as Seen by 31 P Nuclear Magnetic Relaxation —On Cation–Anion Coupled Transport in Thiophosphates. *Chemistry of Materials* **31**, 4591-4597, doi:10.1021/acs.chemmater.9b01435 (2019).

49   Zhang, Z., Roy, P.-N., Li, H., Avdeev, M. & Nazar, L. F. Coupled Cation-Anion Dynamics Enhances Cation Mobility in Room Temperature Superionic Solid-State Electrolytes. *Journal of the American Chemical Society*, doi:10.1021/jacs.9b09343 (2019).

50   Rong, Z. *et al.* Fast Mg 2+ diffusion in Mo 3 (PO 4) 3 O for Mg batteries. *Chem Commun* **53**, 7998-8001, doi:10.1039/c7cc02903a PMID - 28664208 (2017).

51   Delaunay, B. Sur la sphère vide. *Bulletin de l'Académie des Sciences de l'URSS. Classe des sciences mathématiques et na*, 793-800 (1934).

52   Daly, P. W. The Tetrahedron Quality Factors of CSDS. *Max-Planck-Institut für Aeronomie* (1994).

53   Perdew, J. P., Burke, K. & Ernzerhof, M. Generalized Gradient Approximation Made Simple. *Phys Rev Lett* **77**, 3865-3868, doi:10.1103/physrevlett.77.3865 PMID - 10062328 (1996).

54   Blöchl, P. E. Projector augmented-wave method. *Phys Rev B* **50**, 17953-17979, doi:10.1103/physrevb.50.17953 PMID - 9976227 (1994).

55   Kresse, G. Efficient iterative schemes for ab initio total-energy calculations using a plane-wave basis set. *Phys Rev B* **54**, 11169-11186, doi:10.1103/physrevb.54.11169 PMID - 9984901 (1996).

56   Jain, A. *et al.* Formation enthalpies by mixing GGA and GGA + U calculations. *Phys Rev B* **84**, 045115, doi:10.1103/physrevb.84.045115 (2011).

57   Miara, L. J., Richards, W. D., Wang, Y. E. & Ceder, G. First-Principles Studies on Cation Dopants and Electrolyte|Cathode Interphases for Lithium Garnets. *Chemistry of Materials* **27**, 4040-4047, doi:10.1021/acs.chemmater.5b01023.

58   He, X., Zhu, Y., Epstein, A. & Mo, Y. Statistical variances of diffusional properties from ab initio molecular dynamics simulations. *Npj Comput Mater* **4**, 18, doi:10.1038/s41524-018-0074-y (2018).